ACS OMEGA

Open Access

http://pubs.acs.org/journal/acsodf

Article

Oxaliplatin-Loaded Mil-100(Fe) for Chemotherapy–Ferroptosis Combined Therapy for Gastric Cancer

Boyao Sun, Xuewei Zheng, Xiaoyu Zhang, Huaiyu Zhang, and Yang Jiang*

Cite This: *ACS Omega* 2024, 9, 16676–16686

Read Online

ACCESS | Metrics & More | Article Recommendations | Supporting Information

ABSTRACT: Oxaliplatin (Oxa) is a commonly used chemotherapy drug in the treatment of gastric cancer, but its toxic side effects and drug resistance after long-term use have seriously limited its efficacy. Loading chemotherapy drugs with nanomaterials and delivering them to the tumor site are common ways to overcome the above problems. However, nanomaterials as carriers do not have therapeutic functions on their own, and the effect of single chemotherapy is relatively limited, so there is still room for progress in related research. Herein, we construct Oxa@Mil-100(Fe) nanocomposites by loading Oxa with a metal–organic framework (MOF) Mil-100(Fe) with high biocompatibility and a large specific surface area. The pore structure of Mil-100(Fe) is conducive to a large amount of Oxa loading with a drug-loading rate of up to 27.2%. Oxa@Mil-100(Fe) is responsive to the tumor microenvironment (TME) and can release Oxa and Fe^{3+} under external stimulation. On the one hand, Oxa can inhibit the synthesis of DNA and induce the apoptosis of gastric cancer cells. On the other hand, Fe^{3+} can clear overexpressed glutathione (GSH) in TME and be reduced to Fe^{2+}, inhibiting the activity of glutathione peroxidase 4 (GPX4), leading to the accumulation of intracellular lipid peroxides (LPO), and at the same time releasing a large number of reactive oxygen species (ROS) through the Fenton reaction, inducing ferroptosis in gastric cancer cells. With the combination of apoptosis and ferroptosis, Oxa@Mil-100(Fe) shows a good therapeutic effect, and the killing effect on gastric cancer cells is obvious. In a nude mouse model of subcutaneous tumor transplantation, Oxa@Mil-100(Fe) shows a significant inhibitory effect on tumor growth, with an inhibition rate of nearly 60%. In addition to its excellent antitumor activity, Oxa@Mil-100(Fe) has no obvious toxic or side effects. This study provides a new idea and method for the combined treatment of gastric cancer.

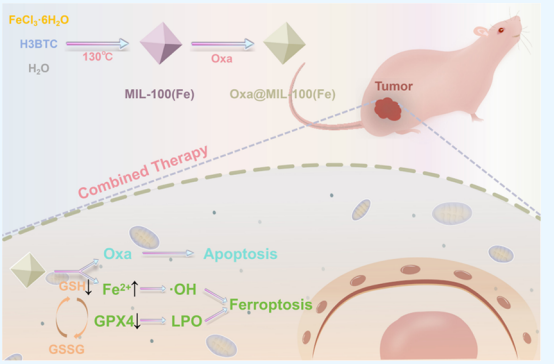

INTRODUCTION

Gastric cancer is a common malignant tumor with the fifth-highest incidence and fourth-highest mortality in the world.[1] Due to the high degree of malignancy, most patients with gastric cancer are at an advanced stage at the time of treatment, and the best time for surgery has been missed. For these patients, chemotherapy is the most commonly used clinical treatment, and oxaliplatin-based drug chemotherapy is the first-line protocol.[2−4] However, traditional chemotherapy involves systemic administration. On the one hand, it is difficult to maintain a high concentration of chemotherapy drugs in the tumor site for a long time, leading to a decrease in the efficacy of chemotherapy and drug resistance in tumor cells. On the other hand, systemic administration may lead to severe side effects and adverse reactions, causing damage to healthy tissues and organs.[5−8] Therefore, it is of great research significance to develop new tumor treatment methods and skillfully combine them with traditional chemotherapy to overcome the limitations of traditional chemotherapy and improve its efficacy at the same time.

The formation of a large number of irregular neovascularization in tumor tissues leads to impaired lymphatic drainage, and macromolecular compounds are highly permeable to tumor tissues and can be retained in tumor tissues, that is, enhanced permeability and retention (EPR) effect.[9−11] Studies have shown that EPR effect can induce the accumulation of not only macromolecular compounds but also many nanomaterials, especially those with particle size between 10 and 400 nm.[12−14] In this context, the method of loading chemotherapy drugs with nanomaterials of appropriate size and delivering them to the tumor sites not only helps to exert the efficacy of chemotherapy drugs but also reduces the toxic and side effects of chemotherapy drugs to a certain extent, showing good development prospects.[15−18] However, relevant studies also face the following problems: (1) the loading rate of chemotherapy drugs is generally low; (2) it is difficult to achieve controlled release of chemotherapy drugs at the tumor sites; and (3) most of the carriers themselves have

Received: January 20, 2024
Revised: February 26, 2024
Accepted: March 19, 2024
Published: April 1, 2024

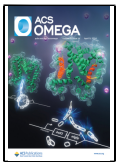

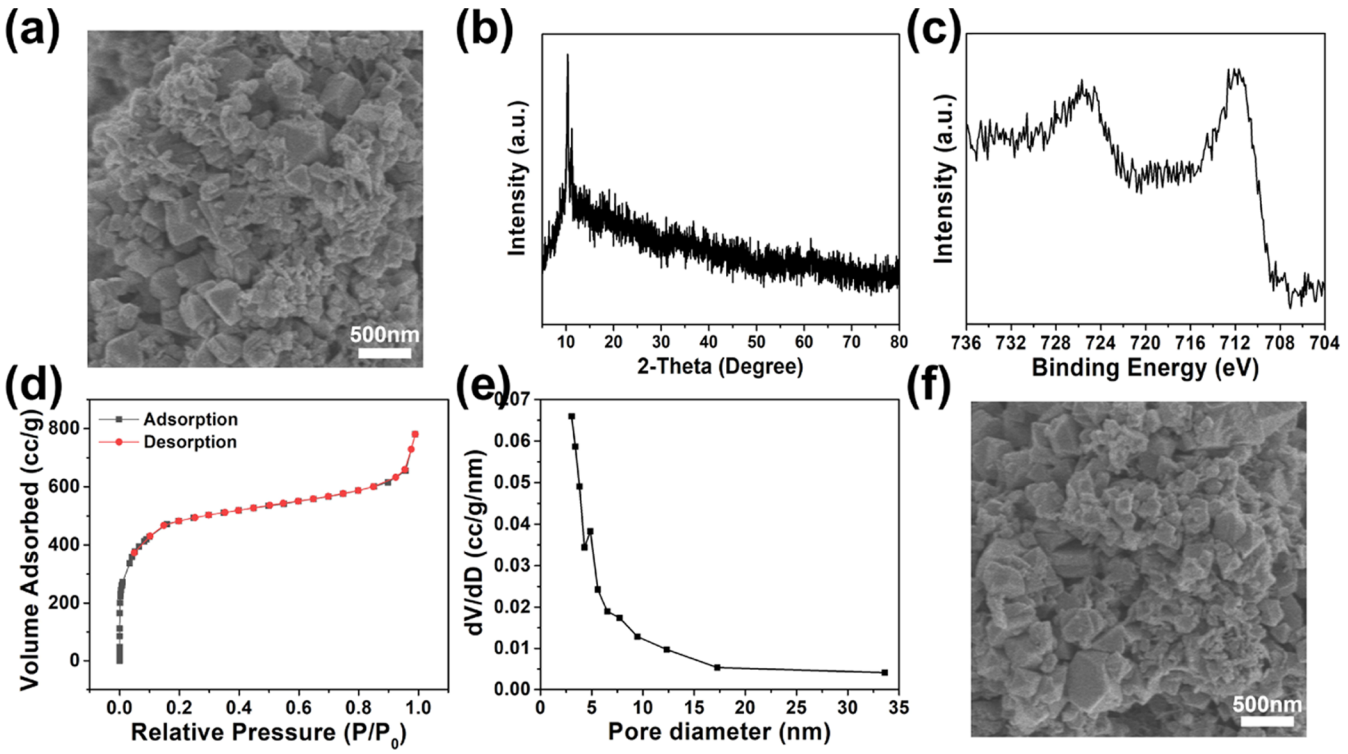

Figure 1. (a) SEM image of Mil-100(Fe). (b) XRD pattern of Mil-100(Fe). (c) XPS Fe 2p spectra of Mil-100(Fe). (d) N_2 adsorption−desorption isotherms of Mil-100(Fe). (e) Pore size distribution of Mil-100(Fe). (f) SEM image of Oxa@Mil-100(Fe).

no therapeutic function, and the effect of single chemotherapy is very limited.

Among many nanomaterials, the metal−organic framework (MOF) structure formed by metal ions and organic ligands through coordination bonds is a new type of porous nanomaterial,[19,20] which has the advantages of large specific surface area,[21] high porosity,[22] adjustable size,[23] and biodegradability,[24] and can be used as a drug carrier, showing good application potential in the biomedical field.[25,26] At present, a variety of MOFs, such as UiO-66,[27] MIL-101,[28] and ZIF-8,[29] have been used for the loading and delivery of chemotherapy drugs. For example, Yin et al. used ZIF-8 as a carrier, loaded with adriamycin and camptothecin, and showed a significant therapeutic effect on drug-resistant liver cancer.[30] In the MOF structure, coordination bonds play a supporting role as a skeleton, and the loading of chemotherapy drugs in MOF is through physical adhesion or hydrogen bonding, $\pi-\pi$ interaction, etc.[31−34] The above-mentioned supramolecular weak interaction is not as stable as a covalent bond, which provides a possibility for the responsive disintegration of the MOF structure and the responsive release of chemotherapy drugs. In addition, ferroptosis-related research has developed rapidly in recent years, and has been well applied in the field of tumor therapy.[35−38] Ferroptosis is an iron-dependent programmed cell death involving intracellular iron accumulation, oxidation−reduction (REDOX) imbalance, and lipid peroxidation.[39−42] Using iron-containing MOF as a chemotherapy drug carrier is also expected to take advantage of the interaction between iron ions and tumor microenvironment (TME) components, resulting in excessive accumulation of lipid peroxides (LPO) and reactive oxygen species (ROS), resulting in a new therapeutic function of ferroptosis.

The responsive disintegration of the MOF structure requires the stimulation of external factors, and TME is an internal environmental network with extremely complex components. It has been reported that a slightly acidic pH value, overexpressed glutathione (GSH), hydrogen peroxide (H_2O_2), and other substances in the TME can destroy the coordination bonds in the structure of MOFs and stimulate their disintegration.[43−46] If an iron-containing MOF is loaded with chemotherapeutic agents, the responsive disintegration of the MOF in the TME can release chemotherapeutic agents and Fe^{3+} ions.[47−49] Chemotherapy drugs can kill tumor cells through specific biological processes and mechanisms, and Fe^{3+} can induce ferroptosis of tumor cells through the clearance of GSH and the generation of Fe^{2+} to achieve the treatment of tumor cells.

Therefore, in this work, we constructed Oxa@Mil-100(Fe) nanocomposites with oxaliplatin (Oxa) loaded onto Mil-100(Fe), a MOF structure with high biocompatibility, large specific surface area, and high porosity. Mil-100(Fe) can load a large amount of Oxa and is responsive to the TME, releasing Oxa and Fe^{3+} into the structure when stimulated. On the one hand, Oxa can inhibit the synthesis of DNA and induce apoptosis of gastric cancer cells.[50] On the other hand, Fe^{3+} can clear overexpressed GSH in the tumor microenvironment and be reduced to Fe^{2+}, inhibit the activity of glutathione peroxidase 4 (GPX4), lead to the accumulation of intracellular LPO, and release a large number of ROS through the Fenton reaction, inducing ferroptosis in gastric cancer cells.[51] Under the combination of apoptosis and ferroptosis, Oxa@Mil-100(Fe) showed a good therapeutic effect, and the killing effect on gastric cancer cells was obvious. In a nude mouse gastric carcinoma subcutaneous transplantation tumor model, Oxa@Mil-100(Fe) showed good antitumor activity and had an obvious inhibitory effect on tumor growth. At the same time, Oxa@Mil-100(Fe) has no obvious toxic or side effects, and the biological safety of the experiment is good. This study provides

https://doi.org/10.1021/acsomega.4c00658
ACS Omega 2024, 9, 16676−16686

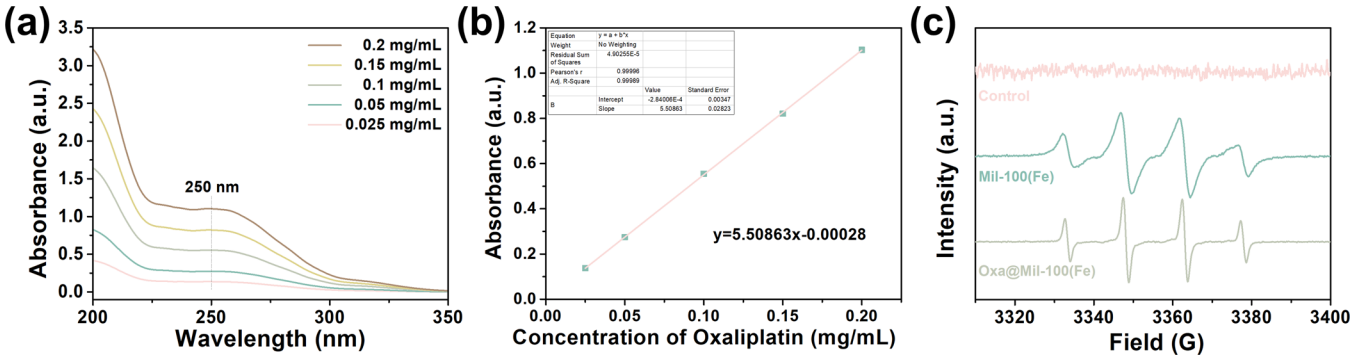

Figure 2. (a) UV−vis absorption spectra for different concentrations of Oxa. (b) Standard absorption curve of Oxa according to the concentration. (c) ESR spectra of different groups under a simulated tumor microenvironment.

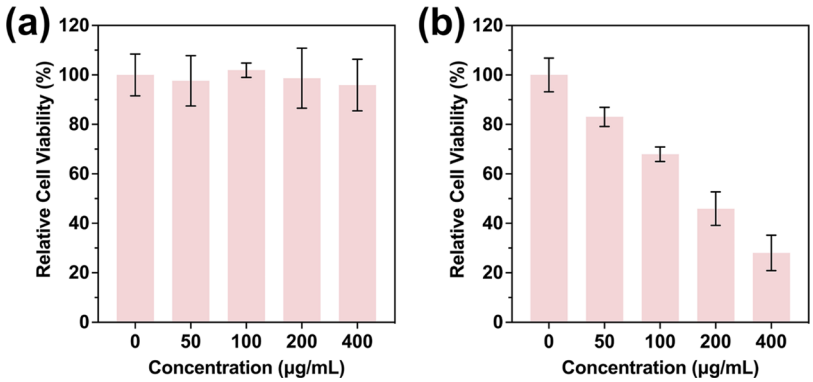

Figure 3. Relative cell viability of GES-1 cells (a) and HGC-27 cells (b) after cocultured with specific concentrations of Oxa@Mil-100(Fe) for 24 h.

a new idea and method for the combined treatment of gastric cancer.

RESULTS AND DISCUSSION

Mil-100(Fe) prepared by the hydrothermal synthesis method showed an irregular morphology, with an average diameter of 278 nm under SEM (Figure 1a). The X-ray diffraction (XRD) patterns showed that the position and intensity of the diffraction peak of the prepared Mil-100(Fe) were very consistent with the standard peak position (Figure 1b). In the X-ray photoelectron spectroscopy (XPS) spectrum, Fe $2p_{3/2}$ was found in the range from 716 to 708 eV, and the characteristic peak at 712 eV represents the connection between Fe and O,[51] which proves that the structure of Mil-100(Fe) is dominated by the coordination of the two (Figure 1c). This confirms the successful preparation of Mil-100(Fe). The N_2 adsorption/desorption isotherms and pore distribution data showed that Mil-100(Fe) contained a large number of pores (Figure 1d,1e). The pores were mainly distributed between 2 and 20 nm, and the mesoporous structure was the main structure. There were also a few pores that exceeded 50 nm, and the macroporous structure was supplemented (Figure 1d). The pore structure greatly improved the specific surface area of Mil-100(Fe), which is 1577 m^2/g, as calculated by the Brunauer−Emmett−Teller (BET) method.

The high pore structure and large surface area of Mil-100(Fe) are conducive to the loading of the chemotherapeutic drug Oxa. The ultraviolet (UV) absorption of Oxa solution with different concentrations was measured (Figure 2a). The absorbance value at 250 nm was used to draw a standard curve of the absorbance value against concentration (Figure 2b). Combined with the UV absorption value of the liquid supernatant of the drug-loading experiment, the drug-loading rate of Oxa was further calculated to be 27.2%. A high drug-loading rate contributed to the achievement of high chemotherapy efficacy. Besides, the loading of Oxa also resulted in a noticeable change in the UV−visible (UV−vis) absorption spectra of Mil-100(Fe) and Oxa@Mil-100(Fe) at around 250 nm (Figure S1). However, the loading of Oxa did not affect the size and morphology of Mil-100(Fe) (Figure 1f). In addition, Mil-100(Fe) and Oxa@Mil-100(Fe) could promote the generation of ROS in a simulated tumor microenvironment solution with a pH of 6.5, GSH concentration of 2 mmol/L, and H_2O_2 concentration of 100 μmol/L. The four characteristic peaks with an intensity ratio of 1:2:2:1 in the ESR spectrum represent the generation of hydroxyl radicals (Figure 2c). However, under normal physiological conditions, Mil-100(Fe) and Oxa@Mil-100(Fe) did not have the ability to generate ROS (Figure S2). On account of the ability of ROS generation in the tumor microenvironment, Mil-100(Fe) and Oxa@Mil-100(Fe) have the potential to induce ferroptosis.

Before the systematic study of antitumor properties, the colloidal stability of Oxa@Mil-100(Fe) was studied first. As shown in Figure S3, before and after 3 days of storage in deionized water, there was almost no significant change in the hydrated particle size of Oxa@Mil-100(Fe) measured by dynamic light scattering (DLS). In addition, in saline, phosphate buffer solution (PBS), RPMI-1640 culture medium, and RPMI-1640 culture medium containing 10% FBS, Oxa@Mil-100(Fe) did not undergo precipitation or aggregation before and after 3 days of incubation, and it was well dispersed with gentle shaking (Figure S4a,b), indicating good colloidal

https://doi.org/10.1021/acsomega.4c00658
ACS Omega 2024, 9, 16676−16686

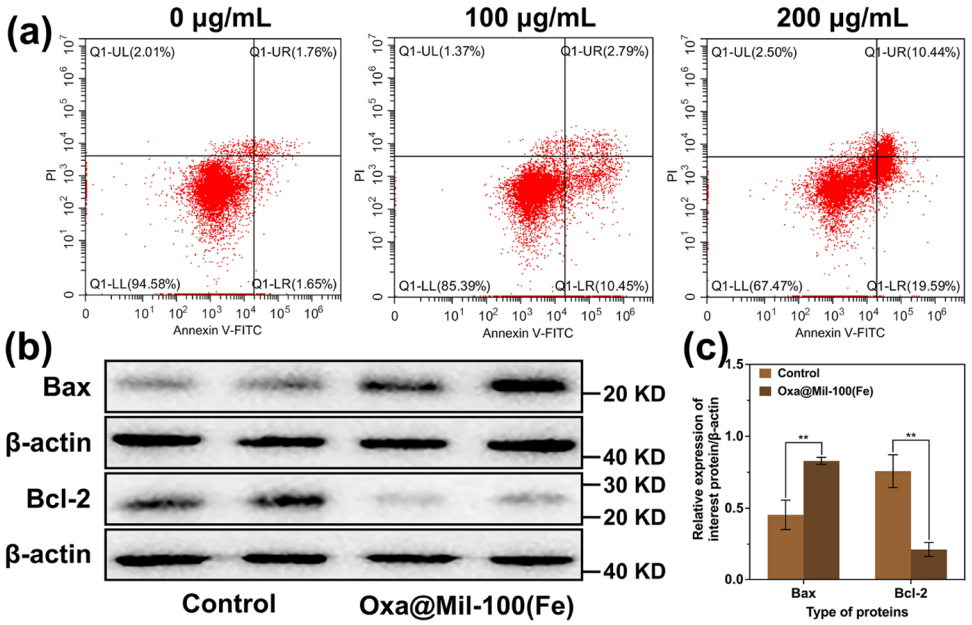

Figure 4. Apoptosis induced by Oxa@Mil-100(Fe) *in vitro*. (a) Cell apoptosis assay after HGC-27 cells were cocultured with 0, 100, and 200 μg/mL Oxa@Mil-100(Fe) for 24 h. (b) The protein expression levels of Bax and Bcl-2 of HGC-27 cells after cocultured with 0 and 200 μg/mL Oxa@Mil-100(Fe) for 24 h. (c) Relative protein expression levels analyzed by ImageJ.

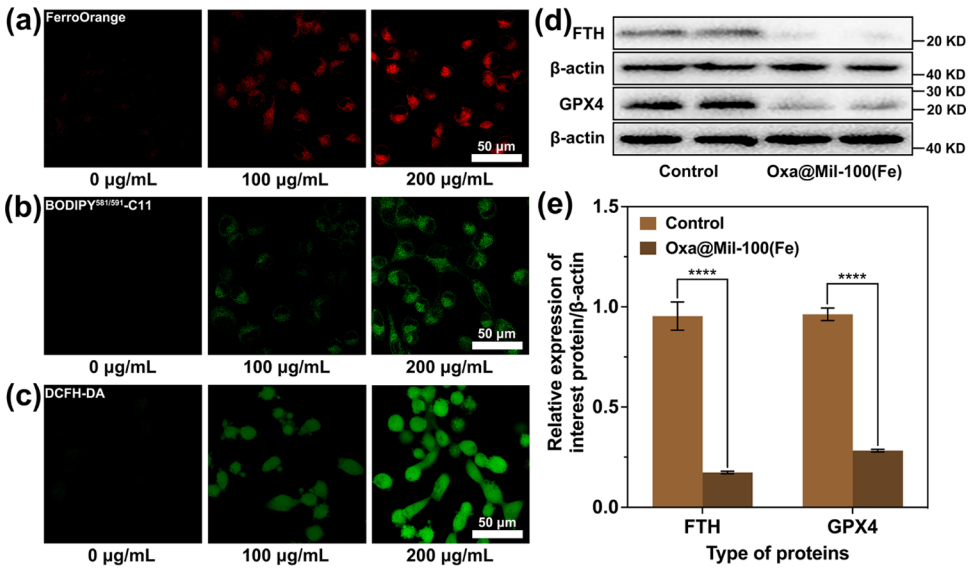

Figure 5. Ferroptosis induced by Oxa@Mil-100(Fe) *in vitro*. CLSM images of FerroOrange (a), BODIPY$^{581/591}$-C11 (b), and DCFH-DA (c) probes in different states in HGC-27 cells after cocultured with 0, 100, and 200 μg/mL Oxa@Mil-100(Fe) for 24 h. The fluorescence intensity in (a–c) reflects the levels of Fe^{2+}, LPO and ROS in HGC-27 cells, respectively. (d) The protein expression levels of FTH and GPX4 in HGC-27 cells after cocultured with 0 and 200 μg/mL Oxa@Mil-100(Fe) for 24 h. (e) The relative protein expression levels were analyzed by ImageJ.

stability in several dispersants involved in subsequent experiments.

Subsequently, in order to verify the antitumor ability of Oxa@Mil-100(Fe), its cytotoxicity was assessed using the CCK-8 assay. It was found that Oxa@Mil-100(Fe) was almost nontoxic to human gastric mucosal cells GES-1 (Figure 3a), whereas it produced higher toxicity in the human gastric cancer cells HGC-27 in a concentration-dependent manner (Figure 3b). After coculture with Oxa@Mil-100(Fe) at 200 μg/mL for 24 h, the relative cellular activity of HGC-27 cells decreased to 45.9% (Figure 3b). The higher toxicity of Oxa@Mil-100(Fe) to HGC-27 cells was due to the stimulation of overexpressed GSH in the tumor microenvironment. As shown in Figure S5, the intracellular GSH content in HGC-27 cells was 2.79 times higher than that in the GES-1 cells. The higher GSH content in the tumor microenvironment resulted in stronger Oxa and Fe^{3+} release (Figure S6b), whereas the release rates of Oxa and Fe^{3+} were significantly slower in normal physiological environments with a lower GSH content (Figure S6a). The destruction of the Oxa@Mil-100(Fe) structure by the tumor microenvironment components leads to the release of Oxa and Fe^{3+}, which can induce apoptosis and ferroptosis of tumor cells at the same time and play an antitumor biological role, which is the most prominent innovation of this work.

On the one hand, it has been reported that Oxa could inhibit the synthesis of DNA and induce the apoptosis of cancer cells.

https://doi.org/10.1021/acsomega.4c00658
ACS Omega 2024, 9, 16676−16686

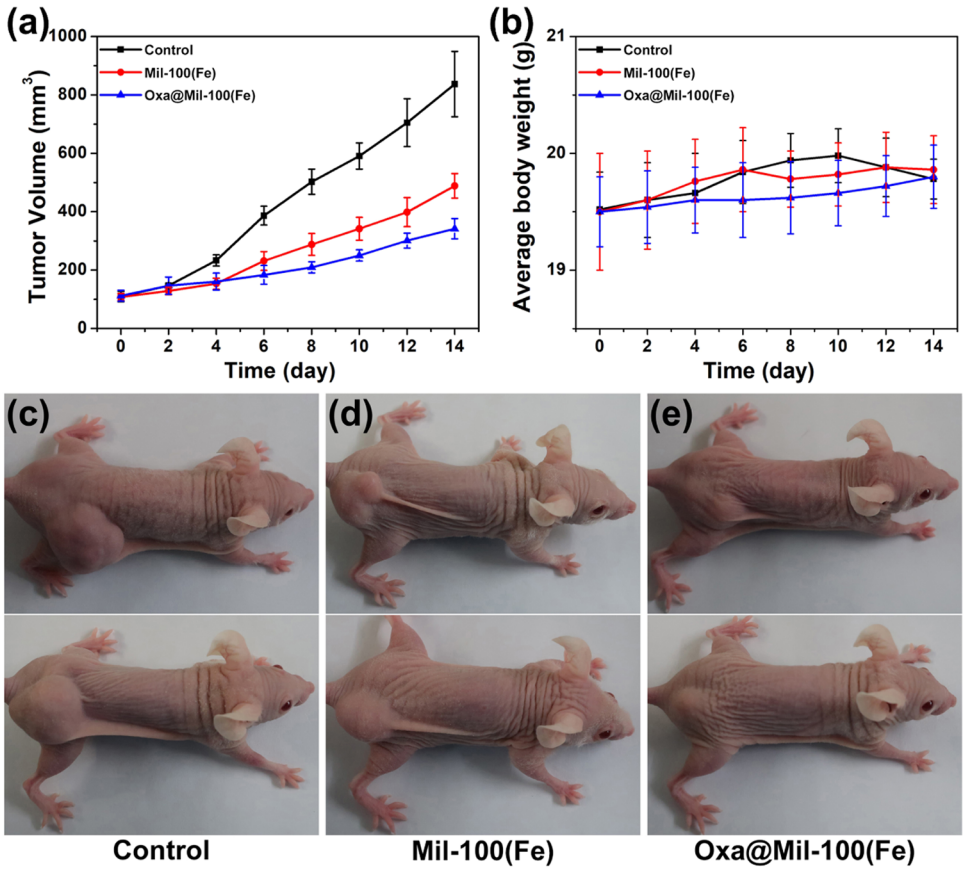

Figure 6. *In vivo* antitumor efficacy of Oxa@Mil-100(Fe). (a) Tumor volume curves of the different groups. (b) Average body weight curves of the different groups. (c−e) Photographs of representative tumor-bearing mice on day 14 after different treatments.

Therefore, the apoptosis of HGC-27 cells was investigated first. As shown in Figure 4a, the number of early and late apoptotic cells gradually increased with increasing concentrations of Oxa@Mil-100(Fe), and the percentages of apoptotic cells were 3.41, 13.24, and 30.03% at Oxa@Mil-100(Fe) concentrations of 0, 100, and 200 μg/mL, respectively. Then, the effect of Oxa@Mil-100(Fe) on the expression of intracellular apoptotic proteins was investigated by Western blotting. After treatment with Oxa@Mil-100(Fe), the expression level of the Bax protein associated with promoting apoptosis was upregulated, while the expression level of the Bcl-2 protein associated with the inhibition of apoptosis was downregulated in HGC-27 cells (Figure 4b). The corresponding quantitative analysis by ImageJ software revealed that the expression level of the Bax protein in HGC-27 cells cocultured with Oxa@Mil-100(Fe) was 1.83 times that in the control group, while the expression level of the Bcl-2 protein was 28% that in the control group (Figure 4c). The above results indicated that apoptosis occurred due to the action of Oxa@Mil-100(Fe) on the HGC-27 cells, and the therapeutic effect of Oxa chemotherapy could be achieved.

On the other hand, Fe^{3+} released by Oxa@Mil-100(Fe) could effectively clear the intracellular GSH. As shown in Figure S7, the content of GSH in HGC-27 cells decreased gradually with an increase of Oxa@Mil-100(Fe) concentration. Fe^{3+} could react with GSH to produce Fe^{2+}, which greatly improved the level of Fe^{2+} in the cells. FerroOrange probe was used for intracellular Fe^{2+} fluorescence imaging, and the relative intensity of the red fluorescence reflected the relative content of Fe^{2+}. Confocal laser scanning microscopy (CLSM) revealed that the content of Fe^{2+} in HGC-27 cells gradually increased with increasing Oxa@Mil-100(Fe) concentration (Figure 5a). The clearance of GSH and the production of Fe^{2+} led to a decrease in GPX4 activity, which further led to the accumulation of intracellular LPO and the release of a large amount of ROS *via* the Fenton reaction. The BODIPY$^{581/591}$-C11 probe was used for intracellular LPO fluorescence imaging, and the relative intensity of green fluorescence reflected the relative content of LPO. As the concentration of Oxa@Mil-100(Fe) increased, the relative content of LPO in HGC-27 cells gradually increased (Figure 5b). The DCFH-DA probe was used for intracellular ROS fluorescence imaging, and the intensity of green fluorescence reflected the relative content of ROS. The relative content of intracellular ROS in HGC-27 cells gradually increased with an increase of Oxa@Mil-100(Fe) concentration (Figure 5c). ImageJ software was used to quantitatively analyze the red or green fluorescence intensity values. Compared with the untreated control group, after coculture with 200 μg/mL Oxa@Mil-100(Fe) for 24 h, the content of Fe^{2+} in HGC-27 cells increased by 4.30 times, the content of LPO increased by 8.86 times, and the content of ROS increased by 3.78 times (Figures S8, S9 and S10). Flow cytometry was also employed to detect the ROS in HGC-27 cells, and a similar result was obtained: Oxa@Mil-100(Fe) could accelerate intracellular ROS production (Figure S11a,b). The above experimental results proved that the two most important signs of ferroptosis, excessive accumulation of LPO and massive production of ROS in HGC-27 cells appeared, and Oxa@Mil-100(Fe) induced ferroptosis in HGC-27 cells.

https://doi.org/10.1021/acsomega.4c00658
ACS Omega 2024, 9, 16676−16686

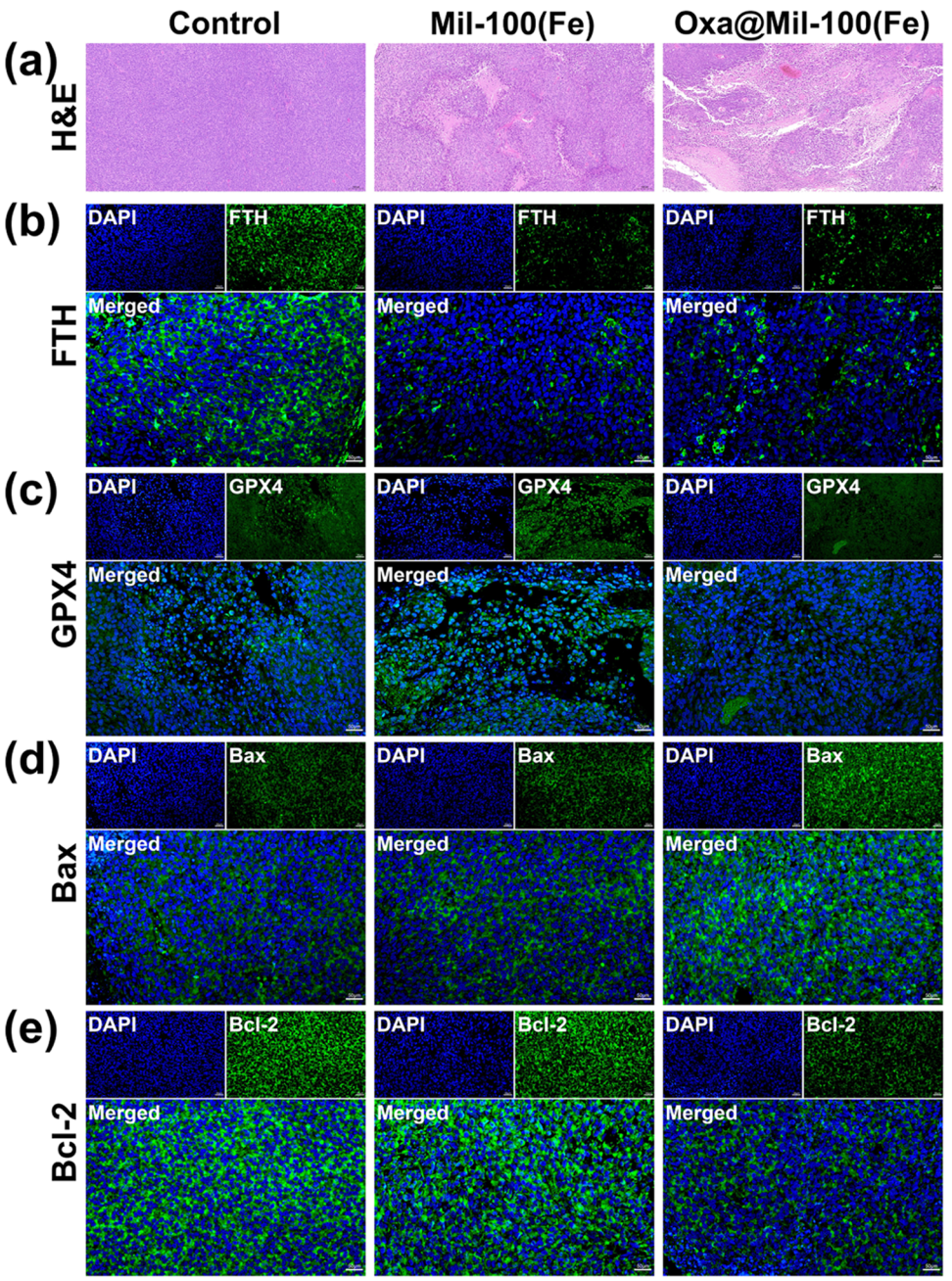

Figure 7. (a) H&E-stained tumor slices from each group. The scale bar is 100 μm. Protein expression was detected by immunofluorescence, including ferroptosis-related proteins (b) FTH and (c) GPX4 and apoptosis-related proteins (d) Bax and (e) Bcl-2. The scale bar is 50 μm.

FTH proteins play a key role in iron metabolism to maintain iron homeostasis, and GPX4 proteins play a key role in maintaining REDOX homeostasis. As important markers in the ferroptosis process, the expression of FTH and GPX4 in HGC-27 cells was also detected by western blotting. It was shown that the levels of FTH and GPX4 proteins were downregulated in HGC-27 cells after Oxa@Mil-100(Fe) treatment (Figure 5d). Compared with the untreated control group, after coculture with 200 μg/mL Oxa@Mil-100(Fe) for 24 h, the contents of FTH and GPX4 in HGC-27 cells decreased to 18.2, and 29.3%, respectively (Figure 5e). The disruption of intracellular iron homeostasis and REDOX homeostasis leads to the downregulation of related protein expression, which again confirms the occurrence of ferroptosis from a biological mechanism.

In addition, both apoptosis and ferroptosis affect the function of mitochondria. Therefore, the mitochondrial membrane potential was examined by CLSM and flow cytometry using the JC-1 probe, whose red fluorescence of aggregates changed to the green fluorescence of monomers when the mitochondrial membrane potential decreased. The CLSM images showed a gradual decrease in the mitochondrial membrane potential of HGC-27 cells as the concentration of Oxa@Mil-100(Fe) increased (Figure S12), and the flow cytometry results were similar (Figure S13). This suggested that Oxa@Mil-100(Fe) caused a change in mitochondrial membrane permeability on HGC-27 cells, disrupting the cellular antioxidant capacity, causing mitochondrial damage, and exerting a positive effect on the development of apoptosis and ferroptosis. By combining chemotherapy and ferroptosis,

https://doi.org/10.1021/acsomega.4c00658
ACS Omega 2024, 9, 16676−16686

Oxa@Mil-100(Fe) showed excellent antitumor effects on HGC-27 cells.

Before investigating the *in vivo* antitumor effects of Oxa@Mil-100(Fe), biocompatibility was first examined by a hemolysis assay. The results showed that no obvious hemolysis occurred after coincubation of erythrocytes with different concentrations of Oxa@Mil-100(Fe) (Figure S14), which indicated that Oxa@Mil-100(Fe) had good biocompatibility. Subsequently, biosafety tests were performed, including routine blood and biochemical examinations (liver and renal functions, ions, blood lipids, and blood glucose). The indexes of the mice injected with Oxa@Mil-100(Fe) were basically at the same level as that of the healthy mice of the same age as the control mice, indicating that the biosafety of Oxa@Mil-100(Fe) was good (Figures S15−S19). H&E staining of the heart, liver, spleen, lungs, and kidneys showed that the cellular morphology and structure of each organ were normal (Figure S20), indicating that Oxa@Mil-100(Fe) had a favorable biosafety profile.

During the 14-day treatment period, the tumors in the control group maintained the fastest growth rate, reaching an average tumor volume of 837 mm^3 after 14 days (Figure 6a,6c). Mil-100(Fe) and Oxa@Mil-100(Fe) showed certain inhibitory effects on tumor growth. The effects of Mil-100(Fe) were due to ferroptosis, with an average tumor volume of 489 mm^3 at day 14 and a tumor inhibition rate of 42% (Figure 6a,6d). The effect of Oxa@Mil-100(Fe) was caused by both chemotherapy and ferroptosis. Under their combined action, the average tumor volume at day 14 was only 342 mm^3, and the tumor inhibition rate was as high as 59% (Figure 6a,6e). Figure 6c−e shows two randomly selected mice from each group, and the size of the tumors once again proves that the combination of chemotherapy and ferroptosis was effective. The body weight of mice in the control group fluctuated, while that in the Mil-100(Fe) and Oxa@Mil-100(Fe) groups showed a steady and continuous increase as a whole, which proved that the growth and development of mice were good and the experiment was safe (Figure 6b).

H&E staining was performed on the anatomically obtained solid tumors, and the results show that the tumor cells in the control group were basically normal. A small number of dead cells appeared in the Mil-100(Fe) group due to ferroptosis. In the Oxa@Mil-100(Fe) group, a large number of tumor cells died, which was the result of the combined effects of chemotherapy and ferroptosis (Figure 7a). To further demonstrate that the *in vivo* antitumor effect of Oxa@Mil-100(Fe) was a combined effect of apoptosis and ferroptosis, immunofluorescence staining was employed to assess the expression of apoptosis- and ferroptosis-related proteins. The results showed that ferroptosis-related GPX4 and FTH proteins were significantly downregulated in the tumor tissues of the Mil-100(Fe) and Oxa@Mil-100(Fe) groups compared to the control group, suggesting that both Mil-100(Fe) and Oxa@Mil-100(Fe) induced ferroptosis *in vivo* (Figure 7b,7c). Meanwhile, apoptosis-related Bax protein was upregulated and Bcl-2 protein was downregulated in the tumor tissues of the Oxa@Mil-100(Fe) group. This indicated that Oxa@Mil-100(Fe) induced apoptosis by releasing Oxa at the tumor sites, while Mil-100(Fe) could not play this role (Figure 7d,7e). The above results indicate that Oxa@Mil-100(Fe) could achieve the combined effect of chemotherapy and ferroptosis while ensuring biosafety, exerting excellent antitumor efficacy *in vivo*.

CONCLUSIONS

Taking advantage of the large surface area, high porosity, and good biocompatibility of the MOF structure, we prepared Oxa@Mil-100(Fe) nanocomposites by using Mil-100(Fe) as the carrier loaded with the chemotherapeutic drug Oxa. Oxa@Mil-100(Fe) is responsive to the tumor microenvironment and is able to release Oxa and Fe^{3+} upon stimulation. On the one hand, Oxa can inhibit the synthesis of DNA and induce apoptosis in gastric cancer cells. On the other hand, Fe^{3+} can clear overexpressed GSH in the tumor microenvironment and be reduced to Fe^{2+}, inhibiting the activity of glutathione peroxidase 4 (GPX4), leading to the accumulation of intracellular LPO, and releasing a large amount of ROS through the Fenton reaction, inducing ferroptosis in gastric cancer cells. With the combination of apoptosis and ferroptosis, Oxa@Mil-100(Fe) showed a good therapeutic effect on gastric cancer cells. In a subcutaneous transplantation tumor model, Oxa@Mil-100(Fe) showed good antitumor activity and had an obvious inhibitory effect on tumor growth. At the same time, Oxa@Mil-100(Fe) has no obvious toxic or side effects. This combination therapy may provide a new strategy for the treatment of gastric cancer.

EXPERIMENTAL SECTION

Materials. $FeCl_3·6H_2O$, 1,3,5-trimesic acid (H3BTC), anhydrous ethanol, and oxaliplatin (Oxa) were purchased from Aladdin. RPMI-1640 medium and fetal bovine serum (FBS) were purchased from Gibco. The human gastric cancer cell line (HGC-27), human gastric mucosa cell line (GES-1), phosphate-buffered saline (PBS), and trypsin-EDTA solution were provided by Servicebio. The cell counting kit-8 (CCK-8) and annexin V-FITC/PI apoptosis analysis kits were purchased from Beijing Solarbio Science & Technology Co., Ltd. GSH and GSSG assay kits, mitochondrial membrane potential assay kit with JC-1, immunostaining permeabilization buffer with Triton X-100, BCA protein assay kit, RIPA lysate, sodium dodecyl sulfate-polyacrylamide gel electrophoresis (SDS-PAGE) sample loading buffer, protease and phosphatase inhibitor cocktail, SDS-PAGE gel quick preparation kit, poly(vinylidene fluoride) (PVDF) membrane, and hypersensitive ECL chemiluminescence kit were purchased from Beyotime. The FerroOrange probe, $BODIPY^{581/591}$-C11 probe, and DCFH-DA probe were purchased from Dojindo. BALB/c nude mice were purchased from Beijing Vital River Laboratory Animal Technology Co., Ltd. Recombinant antiferritin antibody (FTH) and recombinant antiglutathione peroxidase 4 (GPX4) were purchased from Abcam. Recombinant anti-Bax antibody (Bax), recombinant anti-Bcl-2 antibody (Bcl-2), recombinant anti-β-actin antibody (β-actin), and HRP-labeled goat antirabbit IgG H&L were purchased from Proteintech.

Preparation of Mil-100(Fe). 1.622 g of $FeCl_3·6H_2O$ and 1.387 g of H3BTC were added to 5 mL of water. Then, the mixture was transferred to a poly(tetrafluoroethylene)-lined autoclave (25 mL) and reacted at 130 °C for 72 h. After the reaction, the reactor was cooled naturally. Finally, the product was transferred to a centrifuge tube, and centrifuged at a speed of 8000 rpm for 10 min. The solid product obtained after discarding the supernatant was Mil-100(Fe). After washing 2 times with anhydrous ethanol, the prepared Mil-100(Fe) was stored in anhydrous ethanol for further use.

Preparation of Oxa@Mil-100(Fe). An ethanol solution with a concentration of 2 mg/mL Mil-100(Fe) and an ethanol

https://doi.org/10.1021/acsomega.4c00658
ACS Omega 2024, 9, 16676−16686

solution with a concentration of 2 mg/mL Oxa were prepared. The two solutions were mixed in equal volumes and stirred for 24 h in the dark. The product was then transferred to a centrifuge tube, and centrifuged at a speed of 8000 rpm for 10 min. The solid product obtained after discarding the supernatant was Oxa@Mil-100(Fe). After washing 2 times with anhydrous ethanol, the prepared Oxa@Mil-100(Fe) was stored in anhydrous ethanol for further use.

Cytotoxicity Assay. RPMI-1640 medium containing 10% FBS was used for the cell experiments. GES-1 and HGC-27 cells were inoculated in 96-well plates at a density of 10,000 cells per well. After 24 h, the cells were completely attached to the wall, and the culture medium was replaced with a culture medium containing Oxa@Mil-100(Fe) at concentrations of 0, 50, 100, 200, and 400 μg/mL for another 24 h. The optical density (OD) value at 450 nm of each well was determined using a microplate reader using the CCK-8 method, and the relative viability of the cells was calculated.

Intracellular GSH Assay. HGC-27 cells were inoculated into 6-well plates at a density of 300,000 cells per well. After 24 h, the cells were completely attached to the wall, and the culture medium was replaced with a culture medium containing Oxa@Mil-100(Fe) at concentrations of 0, 100, and 200 μg/mL for another 24 h. The intracellular GSH content in each group was detected using GSH and GSSG assay kits.

Intracellular Fe^{2+} Assay. HGC-27 cells were inoculated in confocal cell culture dishes at a density of 150,000 cells per dish. After 24 h, the cells were completely attached to the wall, and the culture medium was replaced with a culture medium containing Oxa@Mil-100(Fe) at concentrations of 0, 100, and 200 μg/mL for another 24 h. After washing with serum-free RPMI-1640 medium and adding 1 mL of FerroOrange probe at a concentration of 1 mmol/L to each dish, the dishes were incubated in a thermostatic incubator for 30 min in the dark. Intracellular Fe^{2+} levels were observed using CLSM at an excitation wavelength of 543 nm.

Mitochondrial Membrane Potential Assay. HGC-27 cells were inoculated in confocal cell culture dishes at a density of 150,000 cells per dish and incubated for 24 h. After 24 h, the cells were completely attached to the wall, and the culture medium was replaced with a culture medium containing Oxa@Mil-100(Fe) at concentrations of 0, 100, and 200 μg/mL for another 24 h. After washing with serum-free RPMI-1640 medium and adding a mixture of 0.5 mL medium and 0.5 mL JC-1 working solution to each dish, the dishes were incubated in a thermostatic incubator for 20 min in the dark. The dishes were washed with JC-1 staining buffer and then observed using CLSM at excitation wavelengths of 490 and 525 nm. Quantitative analysis was performed by using flow cytometry.

Cellular Lipid Hydroperoxide Assay. HGC-27 cells were inoculated in confocal cell culture dishes at a density of 150,000 cells per dish. After 24 h, the cells were completely attached to the wall, and the culture medium was replaced with a culture medium containing Oxa@Mil-100(Fe) at concentrations of 0, 100, and 200 μg/mL for another 24 h. After washing with serum-free RPMI-1640 medium and adding 1 mL of BODIDPY$^{581/591}$-C11 probe at a concentration of 2 mmol/L to each dish, the dishes were incubated in a thermostatic incubator for 30 min in the dark. The intracellular LPO levels were observed using CLSM at an excitation wavelength of 488 nm.

Cellular ROS Assay. HGC-27 cells were inoculated in confocal cell culture dishes at a density of 150,000 cells per dish. After 24 h, the cells were completely attached to the wall, and the culture medium was replaced with a culture medium containing Oxa@Mil-100(Fe) at concentrations of 0, 100, and 200 μg/mL for another 24 h. After washing with serum-free RPMI-1640 medium and adding 1 mL of DCFH-DA probe at a concentration of 10 μmol/L to each dish, the dishes were incubated in a thermostatic incubator for 30 min in the dark. The intracellular ROS levels were observed using CLSM at an excitation wavelength of 488 nm. Quantitative analysis was performed using flow cytometry.

Apoptosis Assay. HGC-27 cells were inoculated in 6-well plates at a density of 300,000 cells per well. After 24 h, the cells were completely attached to the wall, and the culture medium was replaced with a culture medium containing Oxa@Mil-100(Fe) at concentrations of 0, 100, and 200 μg/mL for another 24 h. The cells were collected after washing with PBS. Then, the cells were resuspended in a buffer for staining with Annexin V-FITC and PI and analyzed by flow cytometry.

Western Blotting. HGC-27 cells were inoculated in 6-well plates at a density of 300,000 cells per well. After 24 h, the cells were completely attached to the wall, and the culture medium was replaced with a culture medium containing Oxa@Mil-100(Fe) at concentrations of 0, 100, and 200 μg/mL for another 24 h. The cells were washed twice with ice-cold PBS, and RIPA lysate containing 1% protease inhibitor and 1% phosphatase inhibitor was added. Then, cells were collected and centrifuged, and the supernatant was used as the protein sample, which was assayed by the BCA method to determine the protein concentration of the sample. Protein samples were diluted to the same concentration with an SDS-PAGE upload buffer. Then, a metal bath treatment (100 °C, 10 min) was performed to completely denature and depolymerize them. Sequentially, electrophoretic membrane transfer, closure, incubation with primary and secondary antibodies, and PVDF membranes were photographed using a fully automated chemiluminescence imaging system.

Hemolysis Assay. A 2% percent red blood cells (RBCs) of mice were mixed with final concentrations of 0, 100, 250, 500, and 1000 μg/mL Oxa@Mil-100(Fe). The samples were incubated in a 37 °C water bath for 1 h. Triton X-100 and PBS buffer were used as positive and negative controls, respectively. After incubation, all of the samples were centrifuged at 3000 rpm for 10 min. The supernatant was collected, and the OD value at 570 nm was measured using a microplate reader to calculate the hemolysis rate according to the formula Hemolysis Ratio (%) = $(OD_{sample} - OD_{negative})/(OD_{positive} - OD_{negative}) \times 100\%$.

Safety *In Vivo*. 50 μL of Oxa@Mil-100(Fe) solution (5 mg/mL) was injected into 15 healthy nude mice *via* the tail vein. Another 15 healthy nude mice were injected with the same dose of saline as the control group. After 1 day of injection, 5 mice were randomly selected from the control and experimental groups, and whole blood was collected for routine blood examination. After 7 days of injection, 5 mice were randomly selected from the control and experimental groups, and whole blood was collected and centrifuged to obtain serum for biochemical examination. After 14 days of injection, the remaining 5 mice in the control and experimental groups were euthanized, and the major organs were dissected and stained with H&E for further histological observation.

https://doi.org/10.1021/acsomega.4c00658
ACS Omega 2024, 9, 16676−16686

Animal Experiments. All animal experiments in this work were approved by the Animal Ethics Committee of the First Hospital of Jilin University. To construct a subcutaneous transplanted tumor model of gastric cancer, 1×10^7 HGC-27 cells in 200 μL of PBS were injected subcutaneously into the right buttocks of the mice. When the tumor volume ($V = (L \times S^2)/2$, where L is the long axis and S is the short axis of the tumor) reached 100 mm^3, the mice were randomly divided into three groups: the control group, Mil-100(Fe) group, and Oxa@Mil-100(Fe) group. A 100 μL of the corresponding solution (at an equivalent concentration of 5 mg/mL Oxa@Mil-100(Fe)) was injected intravenously *via* the tail vein. The body weights and tumor volumes of mice were also recorded. Fourteen days later, the mice were euthanized and dissected to obtain tumors for H&E staining. Immunofluorescence staining was also performed to assess the expression of proteins associated with ferroptosis (FTH and GPX4) and apoptosis (Bax and Bcl-2). Under fluorescence microscopy, the cell nuclei were stained blue with DAPI, and the target proteins appeared green.

Statistical Analysis. Fluorescence intensity and gray value analyses were performed using ImageJ software, and all data are expressed as mean ± standard deviation. The *t*-test was used for comparisons between two groups, and one-way ANOVA was used to test the statistical differences for multiple group comparisons, which were expressed as $P < 0.05$ (*), $P < 0.01$ (**), $P < 0.001$ (***), and $P < 0.0001$ (****).

Characterization. SEM images were obtained using a Hitachi Regulus 8100 scanning electron microscope. X-ray diffraction (XRD) images were obtained using a Palytical B.V. Empyrean X-ray diffractometer. X-ray photoelectron spectroscopy (XPS) spectra were obtained using a PREVAC R3000 X-ray photoelectron spectroscope. Optical density (OD) values were obtained using an RT-6000 microplate reader. Confocal laser scanning microscope (CLSM) images were obtained with an Olympus FV3000 microscope. Western blot bands were visualized using a Tanon 5200 automatic chemiluminescence image analysis system. Flow cytometry analysis was performed using a Beckman Coulter CytoFLEX flow cytometer. H&E staining images were obtained using an OTICS BDS300 inverted microscope.

■ ASSOCIATED CONTENT

Supporting Information

The Supporting Information is available free of charge at https://pubs.acs.org/doi/10.1021/acsomega.4c00658.

> Additional colloidal stability; relative GSH content; quantitative analysis of intracellular Fe^{2+}; LPO and ROS, mitochondrial membrane potential, hemolytic test, routine blood examination, blood biochemical analysis, and H&E-stained organ slices (PDF)

■ AUTHOR INFORMATION

Corresponding Author

Yang Jiang − *Department of Gastrointestinal and Colorectal Surgery, China-Japan Union Hospital of Jilin University, Changchun 130031, P. R. China;* orcid.org/0000-0002-1230-2204; Email: jiangyang@jlu.edu.cn

Authors

Boyao Sun − *Department of Gastrointestinal and Colorectal Surgery, China-Japan Union Hospital of Jilin University, Changchun 130031, P. R. China*

Xuewei Zheng − *Department of Radiology, China-Japan Union Hospital of Jilin University, Changchun 130031, P. R. China*

Xiaoyu Zhang − *Department of Gastrointestinal and Colorectal Surgery, China-Japan Union Hospital of Jilin University, Changchun 130031, P. R. China*

Huaiyu Zhang − *Department of Rehabilitation Medicine, China-Japan Union Hospital of Jilin University, Changchun 130031, P. R. China*

Complete contact information is available at: https://pubs.acs.org/10.1021/acsomega.4c00658

Author Contributions

Y.J. proposed and supervised the project. Y.J. and B.S. designed and performed the experiments. B.S. wrote the paper. X. Z., X.Z., and H.Z. participated in most experiments. All authors have given approval to the final version of the manuscript.

Notes

The authors declare no competing financial interest.

■ ACKNOWLEDGMENTS

This study was supported by the Natural Science Foundation of Jilin Province (20200201430JC) and the Project from the Development and Reform Commission of Jilin Province (2021C043-9).

■ REFERENCES

(1) Sung, H.; Ferlay, J.; Siegel, R. L.; Laversanne, M.; Soerjomataram, I.; Jemal, A.; Bray, F. Global cancer statistics 2020: GLOBOCAN estimates of incidence and mortality worldwide for 36 cancers in 185 countries. *CA: Cancer J. Clin.* **2021**, *71*, 209−249.

(2) Smyth, E. C.; Nilsson, M.; Grabsch, H. I.; van Grieken, N. C. T.; Lordick, F. Gastric cancer. *Lancet* **2020**, *396*, 635−648.

(3) Ajani, J. A.; D'Amico, T. A.; Bentrem, D. J.; Chao, J.; Cooke, D.; Corvera, C.; Das, P.; Enzinger, P. C.; Enzler, T.; Fanta, P.; Farjah, F.; Gerdes, H.; Gibson, M. K.; Hochwald, S.; Hofstetter, W. L.; Ilson, D. H.; Keswani, R. N.; Kim, S.; Kleinberg, L. R.; Klempner, S. J.; Lacy, J.; Ly, Q. P.; Matkowskyj, K. A.; McNamara, M.; Mulcahy, M. F.; Outlaw, D.; Park, H.; Perry, K. A.; Pimiento, J.; Poultsides, G. A.; Reznik, S.; Roses, R. E.; Strong, V. E.; Su, S.; Wang, H. L.; Wiesner, G.; Willett, C. G.; Yakoub, D.; Yoon, H.; McMillian, N.; Pluchino, L. A. Gastric Cancer, Version 2.2022, NCCN Clinical Practice Guidelines in Oncology. *J. Natl. Compr. Cancer Netw.* **2022**, *20*, 167−192, DOI: 10.6004/jnccn.2022.0008.

(4) Wagner, A. D.; Syn, N. L. X.; Moehler, M.; Grothe, W.; Yong, W. P.; Tai, B.-C.; Ho, J.; Unverzagt, S. Chemotherapy for advanced gastric cancer. *Cochrane Database Syst. Rev.* **2017**, *2017*, No. CD004064.

(5) Zedan, A. H.; Hansen, T. F.; Svenningsen, A. F.; Vilholm, O. J. Oxaliplatin-Induced Neuropathy in Colorectal Cancer: Many Questions With Few Answers. *Clin. Colorectal Cancer* **2014**, *13*, 73−80.

(6) Sun, Y.; Xie, Y.; Tang, H.; Ren, Z.; Luan, X.; Zhang, Y.; Zhu, M.; Lv, Z.; Bao, H.; Li, Y.; Liu, R.; Shen, Y.; Zheng, Y.; Pei, J. In vitro and in vivo Evaluation of a Novel Estrogen-Targeted PEGylated Oxaliplatin Liposome for Gastric Cancer. *Int. J. Nanomed.* **2021**, *16*, 8279−8303.

(7) Xiao, Y.-F.; Li, B.-S.; Liu, J.-J.; Wang, S.-M.; Liu, J.; Yang, H.; Hu, Y.-Y.; Gong, C.-L.; Li, J.-L.; Yang, S.-M. Role of lncSLCO1C1 in gastric cancer progression and resistance to oxaliplatin therapy. *Clin. Transl. Med.* **2022**, *12*, No. e691.

(8) Rodríguez, F.; Caruana, P.; De la Fuente, N.; Espanol, P.; Gamez, M.; Balart, J.; Llurba, E.; Rovira, R.; Ruiz, R.; Martin-Lorente, C.; Corchero, J. L.; Cespedes, M. V. Nano-Based Approved Pharmaceuticals for Cancer Treatment: Present and Future Challenges. *Biomolecules* **2022**, *12*, No. 784, DOI: 10.3390/biom12060784.
(9) Zhang, M.; Jin, H.; Liu, Y.; Wan, L.; Liu, S.; Zhang, H. L-Arginine self-delivery supramolecular nanodrug for NO gas therapy. *Acta Biomater.* **2023**, *169*, 517−529.
(10) Maeda, H.; Wu, J.; Sawa, T.; Matsumura, Y.; Hori, K. Tumor vascular permeability and the EPR effect in macromolecular therapeutics: a review. *J. Controlled Release* **2000**, *65*, 271−284.
(11) Wu, J. The Enhanced Permeability and Retention (EPR) Effect: The Significance of the Concept and Methods to Enhance Its Application. *J. Pers. Med.* **2021**, *11*, No. 771, DOI: 10.3390/jpm11080771.
(12) Akbari, P.; Taebpour, M.; Akhlaghi, M.; Hasan, S. H.; Shahriyari, S.; Parsaeian, M.; Haghirosadat, B. F.; Rahdar, A.; Pandey, S. Regulation of the P53 tumor suppressor gene and the Mcl-2 oncogene expression by an active herbal component delivered through a smart thermo-pH-sensitive PLGA carrier to improve Osteosarcoma treatment. *Med. Oncol.* **2024**, *41*, No. 68, DOI: 10.1007/s12032-023-02291-4.
(13) Dreher, M. R.; Liu, W. G.; Michelich, C. R.; Dewhirst, M. W.; Yuan, F.; Chilkoti, A. Tumor vascular permeability, accumulation, and penetration of macromolecular drug carriers. *JNCI, J. Natl. Cancer Inst.* **2006**, *98*, 335−344.
(14) Karami, M. H.; Abdouss, M.; Rahdar, A.; Pandey, S. Graphene quantum dots: Background, synthesis methods, and applications as nanocarrier in drug delivery and cancer treatment: An updated review. *Inorg. Chem. Commun.* **2024**, *161*, No. 112032.
(15) Liu, S.; Shen, C.; Qian, C.; Wang, J.; Wang, Z.; Tang, X.; Zhang, Q.; Pan, C.; Ye, W. A Rapid Dual-Responsive Releasing Nano-Carrier by Decomposing the Copolymer and Reversing the Core Dissolution. *Front. Bioeng. Biotech.* **2021**, *9*, No. 784838.
(16) Hong, T.; Shen, X.; Syeda, M. Z.; Zhang, Y.; Sheng, H.; Zhou, Y.; Xu, J.; Zhu, C.; Li, H.; Gu, Z.; Tang, L. Recent advances of bioresponsive polymeric nanomedicine for cancer therapy. *Nano Res.* **2023**, *16*, 2660−2671.
(17) Low, L. E.; Wu, J.; Lee, J.; Tey, B. T.; Goh, B.-H.; Gao, J.; Li, F.; Ling, D. Tumor-responsive dynamic nanoassemblies for targeted imaging, therapy and microenvironment manipulation. *J. Controlled Release* **2020**, *324*, 69−103.
(18) Khanna, N.; Chatterji, T.; Singh, S.; Pandey, S. Application of stimuli responsive nanocomposites in drug delivery and theranostics to counter cancer proliferation and drug resistance. *J. Drug Delivery Sci. Technol.* **2023**, *88*, No. 104958.
(19) Sun, Y.; Zheng, L.; Yang, Y.; Qian, X.; Fu, T.; Li, X.; Yang, Z.; Yan, H.; Cui, C.; Tan, W. Metal-Organic Framework Nanocarriers for Drug Delivery in Biomedical Applications. *Nano-Micro Lett.* **2020**, *12*, No. 103, DOI: 10.1007/s40820-020-00423-3.
(20) Cai, W.; Chu, C.-C.; Liu, G.; Wang, Y.-X. J. Metal-Organic Framework-Based Nanomedicine Platforms for Drug Delivery and Molecular Imaging. *Small* **2015**, *11*, 4806−4822.
(21) Cui, Y.; Li, B.; He, H.; Zhou, W.; Chen, B.; Qian, G. Metal-Organic Frameworks as Platforms for Functional Materials. *Acc. Chem. Res.* **2016**, *49*, 483−493.
(22) Claes, B.; Boudewijns, T.; Muchez, L.; Hooyberghs, G.; Van der Eycken, E. V.; Vanderleyden, J.; Steenackers, H. P.; De Vos, D. E. Smart Metal-Organic Framework Coatings: Triggered Antibiofilm Compound Release. *ACS Appl. Mater. Interfaces* **2017**, *9*, 4440−4449.
(23) Lei, B.; Wang, M.; Jiang, Z.; Qi, W.; Su, R.; He, Z. Constructing Redox-Responsive Metal-Organic Framework Nanocarriers for Anticancer Drug Delivery. *ACS Appl. Mater. Interfaces* **2018**, *10*, 16698−16706.
(24) di Nunzio, M. R.; Agostoni, V.; Cohen, B.; Gref, R.; Douhal, A. A "Ship in a Bottle" Strategy To Load a Hydrophilic Anticancer Drug in Porous Metal Organic Framework Nanoparticles: Efficient Encapsulation, Matrix Stabilization, and Photodelivery. *J. Med. Chem.* **2014**, *57*, 411−420.
(25) Shu, F.; Lv, D.; Song, X.-L.; Huang, B.; Wang, C.; Yu, Y.; Zhao, S.-C. Fabrication of a hyaluronic acid conjugated metal organic framework for targeted drug delivery and magnetic resonance imaging. *RSC Adv.* **2018**, *8*, 6581−6589.
(26) Lázaro, I. A.; Haddad, S.; Rodrigo-Munoz, J. M.; Orellana-Tavra, C.; del Pozo, V.; Fairen-Jimenez, D.; Forgan, R. S. Mechanistic Investigation into the Selective Anticancer Cytotoxicity and Immune System Response of Surface-Functionalized, Dichloroacetate-Loaded, UiO-66 Nanoparticles. *ACS Appl. Mater. Interfaces* **2018**, *10*, 5255−5268, DOI: 10.1021/acsami.7b17756.
(27) Pourmadadi, M.; Eshaghi, M. M.; Ostovar, S.; Shamsabadipour, A.; Safakhah, S.; Mousavi, M. S.; Rahdar, A.; Pandey, S. UiO-66 metal-organic framework nanoparticles as gifted MOFs to the biomedical application: A comprehensive review. *J. Drug Delivery Sci. Technol.* **2022**, *76*, No. 103758.
(28) Lan, G.; Ni, K.; Xu, Z.; Veroneau, S. S.; Song, Y.; Lin, W. Nanoscale Metal-Organic Framework Overcomes Hypoxia for Photodynamic Therapy Primed Cancer Immunotherapy. *J. Am. Chem. Soc.* **2018**, *140*, 5670−5673.
(29) Xin, J.; Wang, S.; Wang, J.; Wang, J.; Fu, L.; Zhang, L.; Shen, L.; Zhang, Z.; Yao, C. Nanosystem Integrated with Photosensitizer and Novel Targeting Chemotherapy Agent for Gastric Cancer Chemo-Photodynamic Combined Therapy. *J. Biomed. Nanotechnol.* **2018**, *14*, 1430−1447.
(30) Yang, J.-C.; Chen, Y.; Li, Y.-H.; Yin, X.-B. Magnetic Resonance Imaging-Guided Multi-Drug Chemotherapy and Photothermal Synergistic Therapy with pH and NIR-Stimulation Release. *ACS Appl. Mater. Interfaces* **2017**, *9*, 22278−22288.
(31) Yang, J.; Dai, D.; Zhang, X.; Teng, L.; Ma, L.; Yang, Y.-W. Multifunctional metal-organic framework (MOF)-based nanoplatforms for cancer therapy: from single to combination therapy. *Theranostics* **2023**, *13*, 295−323.
(32) Rasheed, T.; Rizwan, K.; Bilal, M.; Iqbal, H. M. N. Metal-Organic Framework-Based Engineered Materials-Fundamentals and Applications. *Molecules* **2020**, *25*, No. 1598, DOI: 10.3390/molecules25071598.
(33) Yang, J.; Yang, Y.-W. Metal-Organic Frameworks for Biomedical Applications. *Small* **2020**, *16*, No. 1906846.
(34) Shashikumar, U.; Joshi, S.; Srivastava, A.; Tsai, P.-C.; Shree, K. D. S.; Suresh, M.; Ravindran, B.; Hussain, C. M.; Chawla, S.; Ke, L.-Y.; Ponnusamy, V. K. Trajectory in biological metal-organic frameworks: Biosensing and sustainable strategies-perspectives and challenges. *Int. J. Biol. Macromol.* **2023**, *253*, No. 127120.
(35) Li, Y.; Liu, J.; Wu, S.; Xiao, J.; Zhang, Z.Ferroptosis: opening up potential targets for gastric cancer treatment.*Mol. Cell. Biochem.* 2023, DOI: 10.1007/s11010-023-04886-x.
(36) Le, J.; Pan, G.; Zhang, C.; Chen, Y.; Tiwari, A. K.; Qin, J.-J. Targeting ferroptosis in gastric cancer: Strategies and opportunities. *Immunol. Rev.* **2024**, *321*, 228−245, DOI: 10.1111/imr.13280.
(37) Chen, Z.; Li, Z.; Li, C.; Huang, H.; Ren, Y.; Li, Z.; Hu, Y.; Guo, W. Manganese-containing polydopamine nanoparticles as theranostic agents for magnetic resonance imaging and photothermal/chemodynamic combined ferroptosis therapy treating gastric cancer. *Drug Delivery* **2022**, *29*, 1201−1211.
(38) Nie, J.; Lin, B.; Zhou, M.; Wu, L.; Zheng, T. Role of ferroptosis in hepatocellular carcinoma. *J. Cancer Res. Clin. Oncol.* **2018**, *144*, 2329−2337.
(39) Dixon, S. J.; Lemberg, K. M.; Lamprecht, M. R.; Skouta, R.; Zaitsev, E. M.; Gleason, C. E.; Patel, D. N.; Bauer, A. J.; Cantley, A. M.; Yang, W. S.; Morrison, B., III; Stockwell, B. R. Ferroptosis: An Iron-Dependent Form of Nonapoptotic Cell Death. *Cell* **2012**, *149*, 1060−1072.
(40) Stockwell, B. R.; Angeli, J. P. F.; Bayir, H.; Bush, A. I.; Conrad, M.; Dixon, S. J.; Fulda, S.; Gascon, S.; Hatzios, S. K.; Kagan, V. E.; Noel, K.; Jiang, X.; Linkermann, A.; Murphy, M. E.; Overholtzer, M.; Oyagi, A.; Pagnussat, G. C.; Park, J.; Ran, Q.; Rosenfeld, C. S.; Salnikow, K.; Tang, D.; Torti, F. M.; Torti, S. V.; Toyokuni, S.;

https://doi.org/10.1021/acsomega.4c00658
ACS Omega 2024, 9, 16676−16686

Woerpel, K. A.; Zhang, D. D. Ferroptosis: A Regulated Cell Death Nexus Linking Metabolism, Redox Biology, and Disease. *Cell* **2017**, *171*, 273−285.
(41) Dröge, W. Free radicals in the physiological control of cell function. *Physiol. Rev.* **2002**, *82*, 47−95.
(42) Zhang, M.; Wang, L.; Jin, H.; Zhao, N.; Liu, Y.; Lan, S.; Liu, S.; Zhang, H. Employing single valency polyphenol to prepare metal-phenolic network antitumor reagents through FeOOH assistance. *J. Controlled Release* **2023**, *358*, 612−625.
(43) Kong, F.; Liang, Z.; Luan, D.; Liu, X.; Xu, K.; Tang, B. A Glutathione (GSH)-Responsive Near-Infrared (NIR) Theranostic Prodrug for Cancer Therapy and Imaging. *Anal. Chem.* **2016**, *88*, 6450−6456.
(44) Liu, J.; Zhang, L.; Lei, J.; Shen, H.; Ju, H. Multifunctional Metal-Organic Framework Nanoprobe for Cathepsin B-Activated Cancer Cell Imaging and Chemo-Photodynamic Therapy. *ACS Appl. Mater. Interfaces* **2017**, *9*, 2150−2158.
(45) Yang, K.; Luo, H.; Zeng, M.; Jiang, Y.; Li, J.; Fu, X. Intracellular pH-Triggered, Targeted Drug Delivery to Cancer Cells by Multifunctional Envelope-Type Mesoporous Silica Nanocontainers. *ACS Appl. Mater. Interfaces* **2015**, *7*, 17399−17407.
(46) Li, J.; Ke, W.; Wang, L.; Huang, M.; Yin, W.; Zhang, P.; Chen, Q.; Ge, Z. Self-sufficing H_2O_2-responsive nanocarriers through tumor-specific H_2O_2 production for synergistic oxidation-chemotherapy. *J. Controlled Release* **2016**, *225*, 64−74.
(47) Lin, Z.; Liao, D.; Jiang, C.; Nezamzadeh-Ejhieh, A.; Zheng, M.; Yuan, H.; Liu, J.; Song, H.; Lu, C. Current status and prospects of MIL-based MOF materials for biomedicine applications. *RSC Med. Chem.* **2023**, *14*, 1914−1933.
(48) Rezaei, M.; Abbasi, A.; Varshochian, R.; Dinarvand, R.; Jeddi-Tehrani, M. NanoMIL-100(Fe) containing docetaxel for breast cancer therapy. *Artif. Cells, Nanomed. Biotechnol.* **2018**, *46*, 1390−1401.
(49) Chen, J.; Wang, Y.; Niu, H.; Wang, Y.; Wu, A.; Shu, C.; Zhu, Y.; Bian, Y.; Lin, K. Metal-Organic Framework-Based Nanoagents for Effective Tumor Therapy by Dual Dynamics-Amplified Oxidative Stress. *ACS Appl. Mater. Interfaces* **2021**, *13*, 45201−45213.
(50) Wang, D.; Lippard, S. J. Cellular processing of platinum anticancer drugs. *Nat. Rev. Drug Discovery* **2005**, *4*, 307−320.
(51) Liu, S.; Zhang, M.; Jin, H.; Wang, Z.; Liu, Y.; Zhang, S.; Zhang, H. Iron-Containing Protein-Mimic Supramolecular Iron Delivery Systems for Ferroptosis Tumor Therapy. *J. Am. Chem. Soc.* **2023**, *145*, 160−170.

https://doi.org/10.1021/acsomega.4c00658
ACS Omega 2024, 9, 16676−16686